Intermediate crack induced debonding in steel beams reinforced with CFRP plates under fatigue loading

Massimiliano Bocciarelli, Pierluigi Colombi*, Tommaso D'Antino, Giulia Fava

Department of Architecture, Built Environment and Construction Engineering, Politecnico Milano 1863, P.zza L. da Vinci, 32, 20133 Milan, Italy

Externally adhesively bonded Carbon Fibre Reinforced Polymers (CFRP) plates are often regarded as an effective technique to strengthen notched steel beams. However, the possible CFRP intermediate debonding may dras-tically reduce the reinforced steel beam strength against fatigue crack propagation. It is assumed that, for the beam geometry and materials under analysis, the fatigue load does not directly cause debonding, but it may trigger steel crack propagation, leading to the onset of debonding. In this paper, analytical and numerical models for elasto-brittle adhesives were proposed to evaluate the stress and strain distribution in the reinforcement for a given crack length. The outcomes of experimental campaigns from the literature were considered to validate the proposed numerical and analytical techniques. A good agreement was found among the analytical, numerical and experimental results in terms of strain distribution in the CFRP material, showing the accuracy of the proposed models. Finally, a parametric analysis was performed to investigate the influence of some parameters on the CFRP strain distribution.

Keywords:
Notched steel beams
Fatigue reinforcement
FRP material
Bond slip analysis
Debonding

1. Introduction

The use of Carbon Fibre Reinforced Polymers (CFRP) as reinforcing materials for retrofitting steel structural elements is nowadays proved to be an efficient technique for strengthening or repairing of steel members (plates or beams) [1]. In particular, CFRP strengthening of undamaged steel elements leads to an increase of the load carrying capacity under monotonic loading with a marginal stiffness increment. On the other hand, CFRP repair of cracked steel elements subjected to cyclic loading may significantly improve the fatigue life since it reduces the stresses at the crack tip, the crack opening displacement and the effective stress range. CFRP materials are even more effective if they are pre-stressed, as compressive stresses are introduced into the reinforced element, reducing the effective stress range and then enhancing the fatigue life.

Concerning the fatigue behaviour of notched steel beams reinforced by using CFRP materials, several experimental campaigns were recently presented. In [2], the influence of crack propagation on the CFRP debonding was analyzed for notched steel beams reinforced by using both non-prestressed and prestressed CFRP strips. In [3], different composite reinforcement types were considered, showing that the reinforcement may postpone crack initiation, reduce the fatigue crack propagation, limit the stiffness decay and decrease the residual deflection. In [4], the experimental outcomes revealed the presence of a debonded area between the steel beam and the reinforcement. Finally, in [5] the cracked steel beams were strengthened using different patch systems and high-strength materials and the reinforcement was attached to the steel beam through adhesive bonding or mechanical anchorage. In particular, adhesively bonded CFRP plates led to the most relevant decrease in the fatigue crack growth rate. In [6], the use of different high-strength reinforcing materials was also experimentally studied. The strengthening significantly increased the member fatigue life not only for the stress redistribution on the cracked steel section but also because it led to a local bridging effect, thus reducing both the crack opening displacement and the stress intensity factor.

All the experimental outcomes also showed that the bond between the composite material and the steel element is the weakest link of the strengthened system. Nonetheless, although debonding at notch location under static or fatigue loads has a significant influence on the CFRP strengthening effectiveness, a limited number of analytical or numerical models were proposed in the literature to estimate the effect of debonding on the fatigue crack growth rate.

1.1. Problem statement

The use of high-stiffness composite materials such as CFRP, is extremely effective for crack bridging in the fatigue retrofit of cracked steel elements, resulting in a relevant decrease of the stresses at the

* Corresponding author.
E-mail address: pierluigi.colombi@polimi.it (P. Colombi).

©2018. This manuscript version is made available under the CC-BY-NC-ND 4.0 license http://creativecommons.org/licenses/by-nc-nd/4.0/
Published Journal Article available at: https://doi.org/10.1016/j.engstruct.2018.04.002

crack tip, of the crack opening displacement and of the effective stress range. On the other hand, the notch introduces stress concentrations, which may eventually trigger interfacial debonding. In addition, it was clearly shown that interfacial debonding has a significant influence on the fatigue life [4].

As well known, the fatigue crack propagation is driven by the stress intensity factor (SIF) range at the crack tip. A modified version of the Paris law is often proposed in the literature in order to investigate the fatigue crack growth of CFRP strengthened steel elements [1]:

$$\frac{da}{dN} = C\cdot(\Delta K_{eff}^{m} - \Delta K_{eff,th}^{m}) \tag{1}$$

where a is the crack size, N is the number of cycles, ΔK_{eff} is the effective SIF range, $\Delta K_{eff,th}$ is the effective threshold SIF range and C and m are material parameters (Paris constants). Besides, the effective stress intensity factor range, ΔK_{eff}, is given by:

$$\Delta K_{eff} = K_{\max} - K_{op} = (1-q)\cdot K_{\max} \tag{2}$$

where q is the effective load ratio while $K_{\max}$ is the stress intensity factor at the maximum loading level. A simple formula was proposed in the literature to evaluate the stress intensity factor of unreinforced cracked I-beams [7]. Based on classical beam theory, it reads:

$$K_I^M = M\sqrt{\frac{\beta_M}{I_s\cdot t_w}\left(\frac{I_s}{I_{cr}}-1\right)} \tag{3}$$

where: M is the bending moment, I_s is the moment of inertia of the steel section, I_{cr} is the moment of inertia of the cracked steel section and t_w is the web thickness. For a section subjected to an axial force the following formula is proposed:

$$K_I^N = N\sqrt{\frac{\beta_N}{A_s\cdot t_w}\left(\frac{A_s}{A_{cr}}-1\right)} \tag{4}$$

where: N is the axial force applied to the centroid of the cracked sec-tion, A_s is the section area and A_{cr} is the area of the cracked steel sec-tion. In Eqs. (3) and (4), β_M and β_N are non-dimensional functions of the crack length and beam geometry for pure bending and axial force, respectively.

Recently, such relationships were extended for CFRP reinforced cracked I-beams [8]. The composite material, in fact, introduces a compressive force, N_s, in the steel beam that is clearly not applied at the centroid of the cracked section (Fig. 1).

According to Fig. 1, it holds:

$$N_s = -N_{f0} \tag{5}$$

where $N_{f,0}$ is the CFRP axial force in the cracked section and:

$$M_s = M - N_{f0}\cdot z \tag{6}$$

In Eq. (6), M_s is the total bending moment acting in the steel section, M is the bending moment induced by external loads and z is the distance between the centroid of the steel beam and the centroid of the CFRP strip. After having introduced the additional bending moment to account for the load eccentricity, the stress intensity factor, K_I, of the reinforced cracked steel beam is finally evaluated by taking into account Eqs. (3)–(6):

$$K_I = (M - N_{f0}\cdot z)\sqrt{\frac{\beta_M}{I_s\cdot t_w}\left(\frac{I_s}{I_{cr}}-1\right)} - N_{f0}\sqrt{\frac{\beta_N}{A_s\cdot t_w}\left(\frac{A_s}{A_{cr}}-1\right)} \tag{7}$$

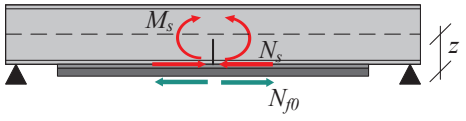

Fig. 1. Axial force acting on the reinforcement and axial force and bending moment acting on the steel beam.

An alternative formulation based on the best fitting of numerical results was proposed in [9]. In Eq. (7), the compressive force N_{f0} strongly affects the stress intensity factor evaluation. Analytical or nu-merical models for evaluating the CFRP axial force are then funda-mental to reliably estimate the fatigue life in retrofitted steel beams. Besides, the slip between the reinforcement and the steel substrate and the possible CFRP debonding should be taken into account.

1.2. Scope of the research

In this paper, reference is made to I-shaped simple supported steel beams. The main aim of this work is to propose both a numerical and an analytical model to evaluate the CFRP axial force in strengthened cracked steel beams. Recently, an analytical model was presented in [10] to provide an estimation of the axial force for long crack lengths, but it was unable to predict the debonded zone length. Besides, a simplified finite element (FE) model was proposed to validate the analytical results [4]. In this work, a more refined numerical analysis employing a cohesive damaged contact interaction is suggested to precisely estimate the CFRP axial force. Additionally, an analytical cohesive zone model is used to evaluate the axial force in the reinforcement together with the debonded zone length. Numerical and analytical analyses are performed for given crack lengths. It is also assumed that, for the adopted reinforced beam geometry and materials, the effect of fatigue load on debonding is negligible. Based on [11], indeed, the fatigue load does not directly influence debonding but it may induce crack propagation in the steel element, resulting then in debonding propagation. The proposed numerical and analytical models are validated with respect to the experimental outcomes presented in [4,12]. Finally, a parametric analysis is performed to investigate the influence of the most significant parameters on the CFRP strain distribution.

1.3. Previous studies

Several analytical and numerical studies were performed with reference to plate end debonding. Analytical solutions were developed assuming an elastic behaviour at the interface between the steel beam and the reinforcement [13,14] or considering a softening interface behaviour and a cohesive crack modelling approach [15]. An energy based analytical formulation was proposed in [16]. In [17], a closed form solution of interfacial stresses and strain was proposed for undamaged FRP-plated steel beams bonded with ductile adhesives. FE models were also presented in [18,19].

Less attention, either analytically or numerically, was devoted in the literature to the evaluation of intermediate crack induced debonding in cracked steel beams reinforced by using CFRP materials. In [20], the interaction between the CFRP debonding and the damage level in the steel beam was considered. Debonding at the damage location was due to stress concentration and the initial damage level influenced the debonding propagation rate. In [21], different levels of initial damage (i.e. notch depth) were considered and a numerical model accounted for both the crack propagation and the CFRP debonding. It turned out that the initial damage level significantly affected the steel beam behaviour and the CFRP debonding. In [22], a model accounting for the bond-slip behaviour of CFRP-steel interface was proposed and experimentally validated. Results of a parametric analysis showed the effectiveness of high modulus reinforcements. In [12], a closed form solution for the interfacial shear and normal stresses in steel beams strengthened with a CFRP plate was presented. A parametric study indicated that the maximum stresses at the notch locations decreased as the adhesive thickness reduced. In [4,10], analytical and numerical models were discussed to predict the CFRP stress redistribution and evaluate the fatigue crack growth curve. A debonded area was experimentally detected and its effect on the fatigue crack growth was captured by the model.

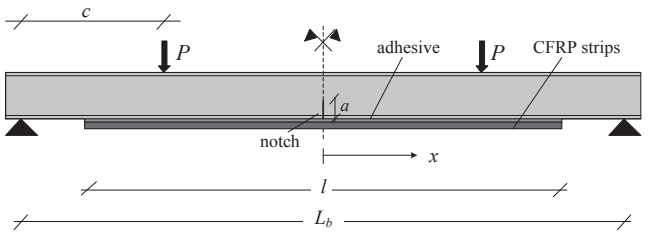

Fig. 2. Simply supported steel I-beam with a crack at midspan under a four-point bending loading configuration.

2. Analytical model

The analytical estimation of the axial force in the reinforcement should account for the interface behaviour between the composite material and the steel substrate. Cohesive zone models were used to study the intermediate debonding of FRP-plated concrete beams [23,24], but, to the authors' knowledge, similar models do not exist for notched steel I-beams. In [12], a theoretical model was discussed but a simply linear interface behaviour was used. A non-linear bond-slip model for the estimation of the debonding process of reinforced steel I-beams is described in the following.

2.1. Governing equations

In this work a simply supported steel I-beam reinforced with CFRP strips is considered (Fig. 2).

The beam is subjected to a four-point bending loading configuration, which is typically adopted in the experimental programs [2,4,12]. A notch in the mid-section of the beam is considered (Fig. 2), but the model can be easily extended for a different loading configuration, geometry or notch location. As usual, both the steel I-beam and the CFRP plate are modelled as linear elastic Euler-Bernoulli beams [10,12]. Besides, the bending stiffness of the reinforcement plate is negligible compared to that of the steel I-beam. It is assumed that the flexural crack introduces local flexibility at the crack location (midspan section) that is conventionally modelled as a rotational spring with infinitesimal thickness [23,24]. For a beam under a bending loading configuration (Fig. 3), the contribution of the cracked section to the strain energy, U, can be evaluated as follows:

$$U = \int_{A^*} \frac{(K_I^M)^2}{E_s} dA \tag{8}$$

where K_I^M is the stress intensity factor due to pure bending moment (Eq.(3)) and E_s is the steel Young's modulus.

In Eq. (8), the term $(K_I^M)^2/E_s$ is the strain energy density for plane stress condition. Eq. (8) can be rewritten as:

$$U = \frac{M^2}{E_s} \int_{A^*} \overline{K}_I^2 dA \tag{9}$$

where:

$$\overline{K}_I = \sqrt{\frac{\beta_M}{I_s \cdot t_w}\left(\frac{I_s}{I_{cr}} - 1\right)} \tag{10}$$

is the stress intensity factor for a unit bending moment. The local flexibility, c^M, at the cracked section is then given by:

$$c^M = \frac{\partial^2 U}{\partial M^2} = \frac{2}{E_s} \int_{A^*} \overline{K}_I^2 dA \tag{11}$$

while the rotational spring stiffness, k^M, is:

$$k^M = \frac{1}{c^M} = \frac{E_s}{2\int_{A^*} \overline{K}_I^2 dA} \tag{12}$$

By discretizing the area A^* (Fig. 3), the rotational spring stiffness can be easily computed numerically. Enforcing the global equilibrium of a given composite beam section (Fig. 4), it holds:

$$\begin{aligned} &N_f \cdot z + M_s + M_f = M \\ &N_s + N_f = 0 \end{aligned} \tag{13}$$

where N_s, M_s, and N_f, M_f are the axial force and bending moment in the steel beam and CFRP reinforcement, respectively. M is the applied bending moment (assuming a null applied axial force), while z is the distance between the centroid of the steel beam and the centroid of the CFRP strip (Fig. 4).

The free body diagram for an infinitesimal portion of the CFRP reinforcement (Fig. 4) gives the following equilibrium equation:

$$N_f' + \tau \cdot b_a = 0 \tag{14}$$

At the steel/adhesive interface, the steel longitudinal displacement u_{sa} is equal to:

$$u_{sa} = u_s + \varphi_s \cdot y_s \tag{15}$$

where u_s and φ_s are the longitudinal displacement and rotation of the centroid of the steel beam section while y_s is the distance from the steel beam centroid to the steel/adhesive interface (Fig. 4). Denoting as u_f the CFRP longitudinal displacement, the relative displacement δ at the steel/adhesive interface is:

$$\delta = u_{sa} - u_f = u_s + \varphi_s \cdot y_s - u_f \tag{16}$$

By differentiating Eq. (16) with respect to x, one has:

$$\delta' = u_s' + \varphi_s' \cdot y_s - u_f' \tag{17}$$

Then, introducing the constitutive relationships for a linear elastic behaviour of steel and CFRP it follows:

$$\begin{aligned} u_s' &= \tfrac{N_s}{E_s A_s} \\ u_f' &= \tfrac{N_f}{E_f A_f} \\ \varphi_s' &= \chi_s = \tfrac{M_s}{E_s I_s} \end{aligned} \tag{18}$$

where χ_s is the steel beam curvature. Neglecting the bending moment M_f in Eq. (13) and substituting Eq. (18) into Eq. (17), one has:

$$\delta' + N_f \left(\frac{1}{E_s A_s} + \frac{1}{E_f A_f} + \frac{z \cdot y_s}{E_s I_s}\right) = \frac{M}{E_s I_s} y_s \tag{19}$$

For the given load configuration (Fig. 2), the bending moment be-tween the applied point loads is constant and equal to M_0 and then Eq. (19) can be rewritten as:

$$\delta' + f_2 \cdot N_f = \Delta\varepsilon_0 \tag{20}$$

where:

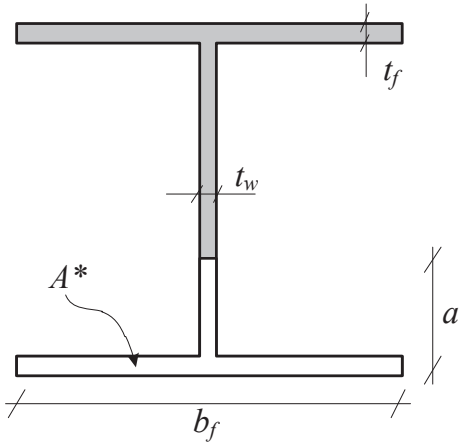

Fig. 3. Section of the cracked I-beam at midspan.

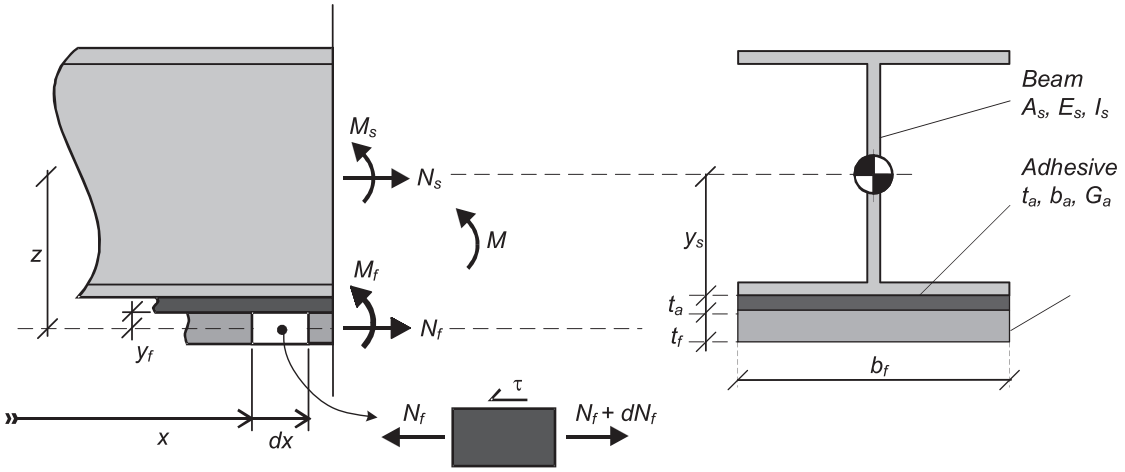

Fig. 4. Notation, sign convention and internal forces in the reinforced steel beam.

$$\Delta\varepsilon_0 = \frac{M}{E_s I_s} y_s = \frac{M_0}{E_s I_s} y_s$$
$$f_2 = \frac{1}{E_s A_s} + \frac{1}{E_f A_f} + \frac{z \cdot y_s}{E_s I_s} \tag{21}$$

In Eq. (21), $\Delta\varepsilon_0$ is the "lack of fit" across the adhesive layer [13,17], while in the expression of f_2 the second term is usually larger than the other ones and then:

$$f_2 \cong \frac{1}{E_f A_f} \tag{22}$$

Differentiating once Eq. (20) with respect to x and applying Eq.(14), it holds:

$$\delta'' - f_2 \cdot b_a \cdot \tau = 0 \tag{23}$$

The interface between the steel and the reinforcement is modelled as a cohesive zone with a given bond-slip law. Several bond slip laws, from elasto-softening law to elasto-brittle law or brittle-softening law, may be considered but the linear or bilinear relationships are usually adopted [23,24].

In this study, an elasto-brittle bond-slip law is adopted (Fig. 5) to describe the brittle behaviour of the adhesive [10,12]. The bond-slip relationship is comprised of two stages, the elastic stage and the failure stage. This means that the elastic limit represents also the onset of debonding since no softening is present. The elasto-brittle relationship between the shear stress, τ, and the slip, δ, is described as:

$$\tau = \begin{cases} k_1 \delta & \text{for} \quad \delta \leqslant \bar{\delta} \\ 0 & \text{for} \quad \delta > \bar{\delta} \end{cases} \tag{24}$$

Such nonlinear relationship contains two material properties: the elastic interface stiffness k_1 and the slip at the debonding $\bar{\delta}$, with $\bar{\tau} = k_1 \bar{\delta}$ being the CFRP-steel interface shear strength. The area under the bond-slip relationship is the fracture energy, G_f:

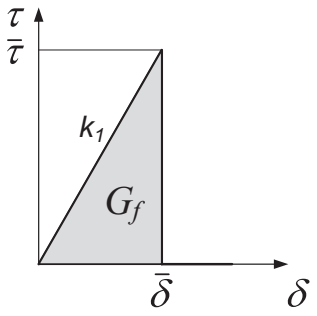

Fig. 5. Elasto-brittle bond-slip relationship.

$$G_f = \int_0^{\bar{\delta}} \tau d\delta = \frac{1}{2} \bar{\tau} \cdot \bar{\delta} \tag{25}$$

The fracture energy can be rewritten as a function of $\bar{\delta}$ and $\bar{\tau}$:

$$G_f = \frac{\bar{\tau}^2}{2k_1} \text{ or } G_f = \frac{k_1 \bar{\delta}^2}{2} \tag{26}$$

2.2. Evaluation of the debonding process

Under the external load, interfacial shear stress develops along the interface between the steel and the CFRP reinforcement. For an applied load higher or equal than a certain limit value, interfacial debonding occurs and propagates along the interface. The interface is divided in two regions, delimited by the flexural crack at midspan and reference is made to the right-hand side of the beam. The steel beam is also divided into two parts that are joined together at the crack location by a flexural spring with a stiffness k^M (Fig. 6).

The following relationships hold between the relative rotation, $\Delta\varphi_{AB}$, and the bending moment, M_s, in the steel beam at the cracked section:

$$\Delta\varphi_{AB} = 2\varphi_B = -2\varphi_A = \frac{M_s}{k^M} \tag{27}$$

According to the bond-slip law described in Eq. (24), two different stages are present along the interface. In the first one (elastic stage), the opening of the flexural crack induces a finite slip between the steel beam and the CFRP, δ_B, which, for an applied moment at the cracked section M_{s0}, is equal to:

$$\delta_B = \varphi_B y_s = \frac{M_{s0}}{2k^M} y_s \tag{28}$$

Stress concentration is then introduced at the interface due to the finite slip. However, in this stage the maximum interface shear stress, τ, is lower than the shear strength $\bar{\tau}$, and the shear stress distribution is sketched in Fig. 6a. As the load rises, the maximum interfacial shear stress increases up to the shear strength $\bar{\tau}$. Then, part of the right-hand interface enters the debonding stage and two different regions exist, namely the elastic region and the debonded zone. The length of the debonded zone, d, and the shear stress distribution are sketched in Fig. 6b.

2.2.1. Elastic stage

In this stage, assuming the bond-slip law in Eq. (24), Eq. (23) can be rewritten as:

$$\delta'' - \lambda^2 \cdot \delta = 0 \tag{29}$$

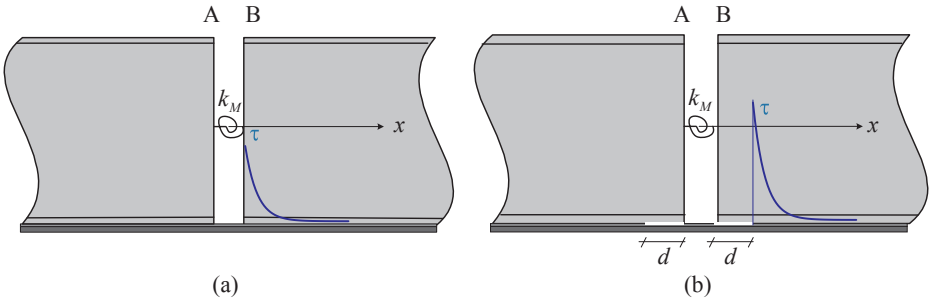

Fig. 6. Model of the beam at crack location: (a) elastic stage and (b) elasto-debonding stage.

where:

$$\lambda^2 = \frac{f_2}{f_1}$$
$$\frac{1}{f_1} = k_1 b_a \tag{30}$$

Substituting Eq. (22) into Eq. (30), it holds:

$$\lambda^2 \cong \frac{k_1 b_a}{E_f A_f} \tag{31}$$

The solution of Eq. (29) is:

$$\delta = C_1 e^{-\lambda x} + C_2 e^{\lambda x} \tag{32}$$

For sufficiently long values of x, the slip is equal to zero and then $C_2 = 0$. Therefore, Eq. (32) becomes:

$$\delta = C_1 e^{-\lambda x} \tag{33}$$

This means that at a sufficiently long distance from the cracked section the strengthened beam behaves as a composite beam. As for the determination of C_1, the following displacement boundary condition is applied at $x = 0$ (the cracked section) starting from Eq. (28):

$$\delta_0 = \frac{M_{s0}}{2k^M} y_s \tag{34}$$

and then:

$$C_1 = \delta_0 \tag{35}$$

At the elastic limit, the bond slip is equal to $\overline{\delta}$ and $C_1 = \overline{\delta}$. The solution for the bond slip, δ_{el}, and the shear stress, τ_{el}, at the elastic limit are:

$$\delta_{el} = \overline{\delta} \cdot e^{-\lambda x}$$
$$\tau_{el} = k_1 \cdot \delta_{el} \tag{36}$$

The axial force in the composite strips at the elastic limit is finally computed from Eq. (20):

$$N_{f,el} = \frac{\Delta\varepsilon_{0,el} + \lambda\overline{\delta} e^{-\lambda x}}{f_2} \tag{37}$$

where $\Delta\varepsilon_{0,el}$ is the lack of fit at the elastic limit (Eq. (21)). To compute the external load, P_{el}, at the elastic limit (onset of debonding), Eq. (34) is firstly rewritten as:

$$\overline{\delta} = \frac{M_{s0,el}}{2k^M} y_s \tag{38}$$

where $M_{s0,el}$ is the bending moment in the steel beam in $x = 0$ at the elastic limit. Neglecting again the bending moment in the CFRP reinforcement, $M_{s0,el}$ is given by Eq. (13) as:

$$M_{s0,el} = M_{0,el} - N_{f0,el} \cdot z \tag{39}$$

where $M_{0,el}$ and $N_{f0,el}$ are respectively the applied bending moment and the CFRP axial force in $x = 0$ at the elastic limit, while $N_{f0,el}$ is computed from Eq. (37):

$$N_{f0,el} = \frac{\lambda\overline{\delta} + \Delta\varepsilon_{0,el}}{f_2} \tag{40}$$

Substituing Eqs. (40) and (39) into Eq. (38), the lack of fit $\Delta\varepsilon_{0,el}$ at the elastic limit is equal to:

$$\Delta\varepsilon_{0,el} = \frac{\overline{\delta}\left(1 + \frac{z y_s \lambda}{2 f_2 k^M}\right)}{\frac{E_s I_s}{2k^M}\left(1 - \frac{z y_s}{f_2 E_s I_s}\right)} \tag{41}$$

and finally the bending moment at the elastic limit, $M_{0,el}$, is given by:

$$M_{0,el} = \frac{\Delta\varepsilon_{0,el} \cdot E_s I_s}{y_s} \tag{42}$$

resulting in an external load, P_{el}, at the elastic limit (onset of debonding) equal to:

$$P_{el} = \frac{M_{0,el}}{c} \tag{43}$$

In the elastic stage, the response is linear with the applied load and then the solution for $P < P_{el}$ is easily evaluated scaling the solution at the elastic limit (Eqs. (36) and (37)) by a factor P/P_{el}.

2.2.2. Elastic-debonding stage

If the load is increased beyond the elastic limit, a debonded region of length d appears at the interface. The right interface is divided into two regions, namely the elastic region ($x > d$) and the debonded region ($x < d$). In the elastic region the solution has the same form as in Eq. (33):

$$\delta = C_3 e^{-\lambda(x-d)} \quad (x > d) \tag{44}$$

The constant C_3 is evaluated by enforcing $\delta = \overline{\delta}$ for $x = d$, which provides $C_3 = \overline{\delta}$. The axial force in the composite strip is evaluated from Eqs. (20) and (44) as:

$$N_f = \frac{\Delta\varepsilon_0 + \lambda\overline{\delta} e^{-\lambda(x-d)}}{f_2} \quad (x > d) \tag{45}$$

where $\Delta\varepsilon_0$ is the lack of fit for $x = 0$ (at the cracked section). The axial force in the composite strip at $x = d$, $N_{f,d}$, is finally computed from Eq. (45):

$$N_{f,d} = \frac{\lambda\overline{\delta} + \Delta\varepsilon_0}{f_2} \tag{46}$$

In the debonded region, $\tau = 0$ and then $\delta'' = 0$ (Eq. (23)). The slip is then linear:

$$\delta = C_4(x-d) + C_5 \quad (x < d) \tag{47}$$

The boundary conditions for Eq. (47) are:

$$\delta = \overline{\delta} \text{ for } x = d$$
$$N_f = N_{f,d} \text{ for } x = d \tag{48}$$

where $N_{f,d}$ is given by Eq. (46). From Eq. (48), it follows:

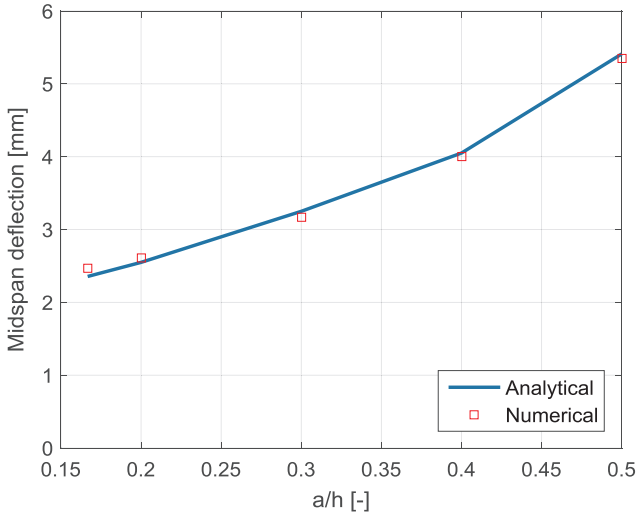

Fig. 7. Midspan deflection of the bare beam: analytical and numerical results.

$$C_5 = \overline{\delta}$$
$$C_4 = -\lambda\overline{\delta} \tag{49}$$

and finally:

$$\delta = -\lambda\overline{\delta}\,(x-d) + \overline{\delta} \quad (x < d) \tag{50}$$

The CFRP axial force in the debonded region is constant and given by Eq. (46).

2.3. Axial strain in the CFRP reinforcement after debonding and at the elastic limit

The axial force in the reinforcement after debonding is given by Eq. (46). From Eqs. (21) and (30) it follows:

$$N_{f,d} = \frac{k_1 b_a \overline{\delta}}{\lambda} + \frac{M_0 y_s}{f_2 E_s I_s} \tag{51}$$

or equivalently from Eq. (24):

$$N_{f,d} = \frac{b_a \overline{\tau}}{\lambda} + \frac{M_0 y_s}{f_2 E_s I_s} \tag{52}$$

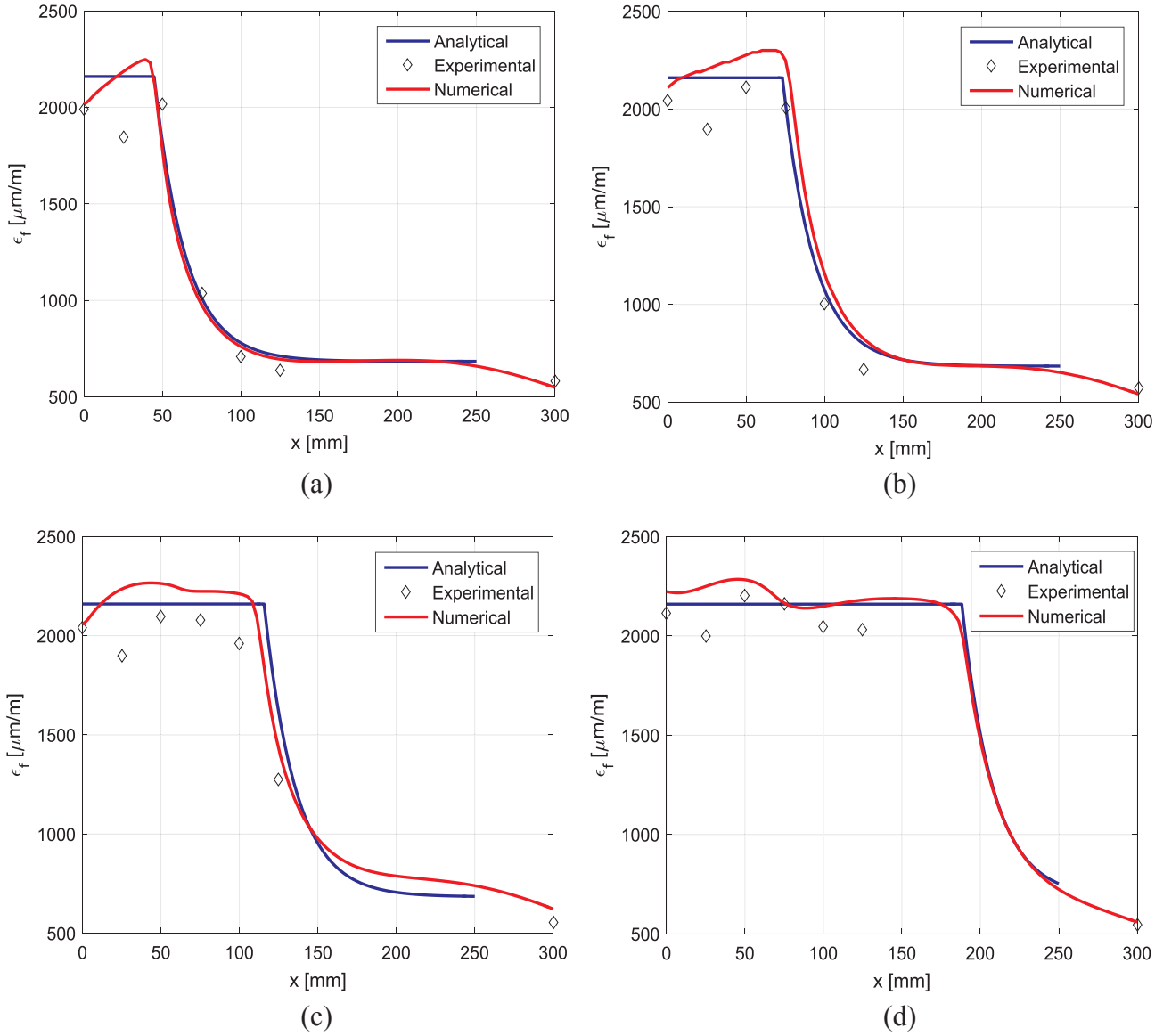

Fig. 8. Analytical, numerical and experimental results for the axial strain distribution in the CFRP reinforcement: (a) $a/h = 0.22$, (b) $a/h = 0.3$, (c) $a/h = 0.4$, (d) $a/h = 0.5$.

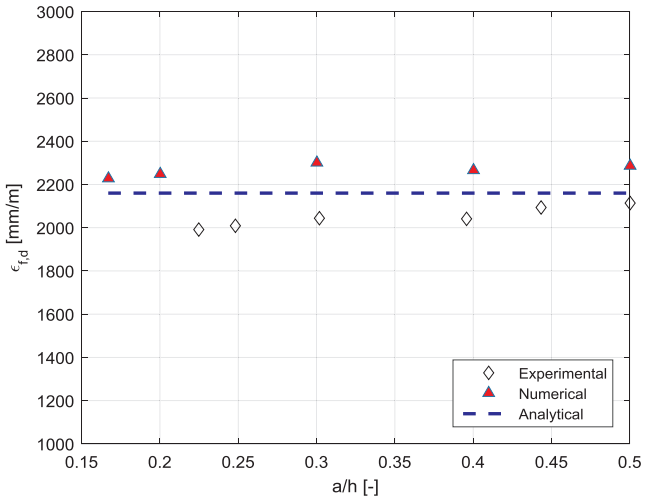

Fig. 9. Longitudinal strain in the debonded zone as function of the normalized crack length a/h: comparison between the experimental [4], numerical and analytical results.

By using Eqs. (25) and (31), $N_{f,d}$ is rewritten in terms of the fracture energy G_f as:

$$N_{f,d} = b_a\sqrt{2G_f E_f t_f} + \frac{M_0 y_s}{f_2 E_s I_s} \tag{53}$$

The axial strain in the reinforcement in the debonded region, $\varepsilon_{f,d}$, is evaluated as (Eq. (22)):

$$\varepsilon_{f,d} = \frac{b_a \bar{\tau}}{\lambda E_f A_f} + \frac{M_0 y_s}{E_s I_s} \tag{54}$$

Again, applying Eqs. (25) and (31), $\varepsilon_{f,d}$ is rewritten in terms of the fracture energy G_f as:

$$\varepsilon_{f,d} = \sqrt{\frac{2G_f}{E_f t_f}} + \frac{M_0 y_s}{E_s I_s} \tag{55}$$

where t_f is the thickness of the composite strip (laminate). Eq. (55) has an interesting physical meaning. It shows that the CFRP axial strain after debonding is the sum of the axial strain associated with the onset of interface debonding (first term) and of the axial strain in the steel beam cross section at the steel/adhesive interface (second term). The axial strain at the elastic limit, $\varepsilon_{f0,el}$, is evaluated as (see Eq. (40)):

$$\varepsilon_{f0,el} = \sqrt{\frac{2G_f}{E_f t_f}} + \frac{M_{0,el} y_s}{E_s I_s} \tag{56}$$

where $M_{0,el}$ is given by Eq. (42). Again, Eq. (56) has an important physical meaning, that is, the CFRP axial strain at the elastic limit (onset of debonding) is equal to the sum of the axial strain associated with the onset of the interface debonding (first term) and of the axial strain in the steel beam cross section at the steel/adhesive interface (second term).

Table 2
Layout of the parametric analyses.

Case	Model parameters					Remarks
	a/h [–]	k_1 [N/mm^3]	E_f [MPa]	G_f [MPa/mm]	$\bar{\tau}$ [MPa]	
1	0.22	584.6	195,000	0.3421	20	Effect of the
2	0.3	584.6	195,000	0.3421	20	normalize crack size
3	0.4	584.6	195,000	0.3421	20	a/h
4	0.5	584.6	195,000	0.3421	20	
5	0.3	400	195,000	0.3421	16.54	Effect of the interface
6	0.3	600	195,000	0.3421	20.26	elastic stiffness k_1
7	0.3	800	195,000	0.3421	23.39	
8	0.3	1000	195,000	0.3421	26.15	
9	0.3	1500	195,000	0.3421	32.03	
10	0.3	584.6	165,000	0.3421	20	Effect of the
11	0.3	584.6	205,000	0.3421	20	reinforcement
12	0.3	584.6	300,000	0.3421	20	Young's modulus E_f
13	0.3	584.6	375,000	0.3421	20	
14	0.3	584.6	440,000	0.3421	20	

2.4. Intermediate debonded zone length

The length of the debonded zone, d, is evaluated by using the analytical model. The slip in the elastic-debonding stage at the cracked section, δ_0, is given by Eq. (50) for $x = 0$:

$$\delta_0 = \lambda\bar{\delta} d + \bar{\delta} \tag{57}$$

The bond slip at $x = 0$ should be equal to:

$$\delta_0 = \frac{M_{s0}}{2k^M} = \frac{M_0 - N_{f,d} z}{2k^M} \tag{58}$$

and then equating Eq. (57) to Eq. (58), the debonded zone length, d, is obtained:

$$d = \frac{\frac{M_0 - N_{f,d} z}{2k^M} - \bar{\delta}}{\lambda\bar{\delta}} \tag{59}$$

where $N_{f,d}$ is given by Eq. (52) or Eq. (53) in terms of the interface shear strength or the fracture energy.

3. Numerical model

3.1. Cohesive models

Debonding of the CFRP reinforcement is investigated in this section using the commercial finite element code Abaqus [25]. All the materials (CFRP reinforcement and steel beam) are considered as linear-elastic, isotropic and homogeneous and they were connected defining a proper interface. Two contact surfaces were defined in the finite element model, both on the CFRP reinforcement and on the steel beam and they were linked through a connection interface. This connection interface was modelled by means of a specific master-slave cohesive damaged contact interaction. Note that the connection interface had zero-thick-ness and the adhesive layer was not explicitly implemented in the finite element model. The mechanical properties of the adhesive layer were taken into account in the definition of the contact properties as illustrated below.

Table 1
Comparison between the experimental results in [12] and the results of the analytical and numerical models discussed in this study.

Specimen	Notch depth [mm]	Reinforcement thickness [mm]	Load at the elastic limit (experimental) [kN]	Load at the elastic limit (analytical) [kN]	Load at the elastic limit (numerical) [kN]
AR-1	14.4	1.4	32	33.7	36.2
AR-2	14.4	1.4	34		
AR-3	14.4	1.4	38		

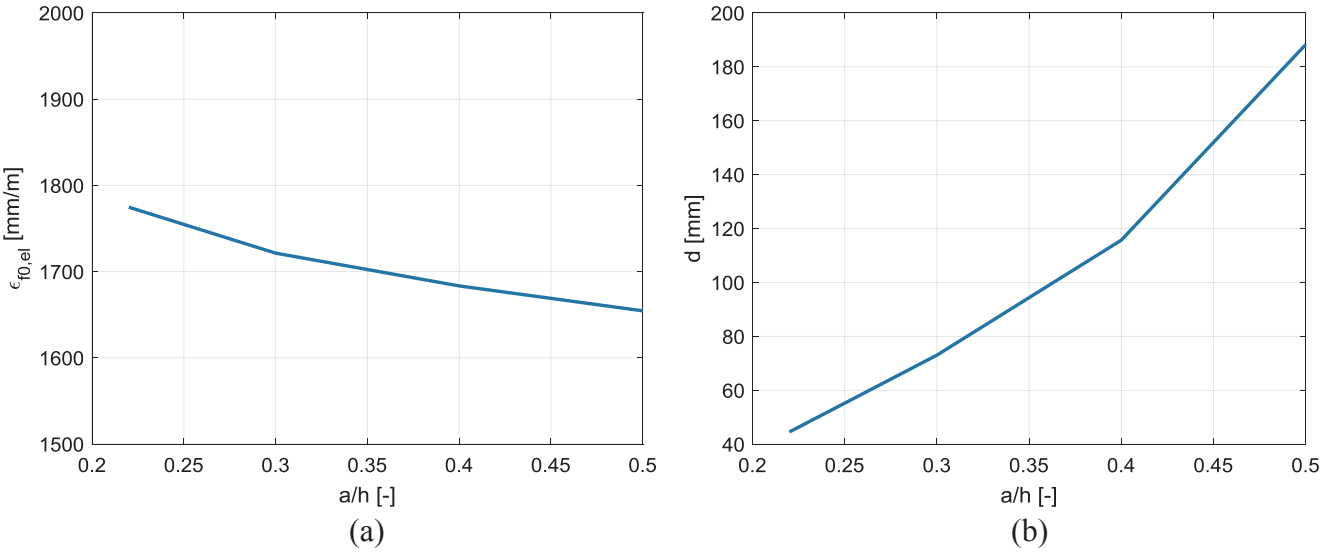

Fig. 10. Effect of the normalized crack length a/h on (a) the CFRP strain at the elastic limit and (b) the length of the debonded zone.

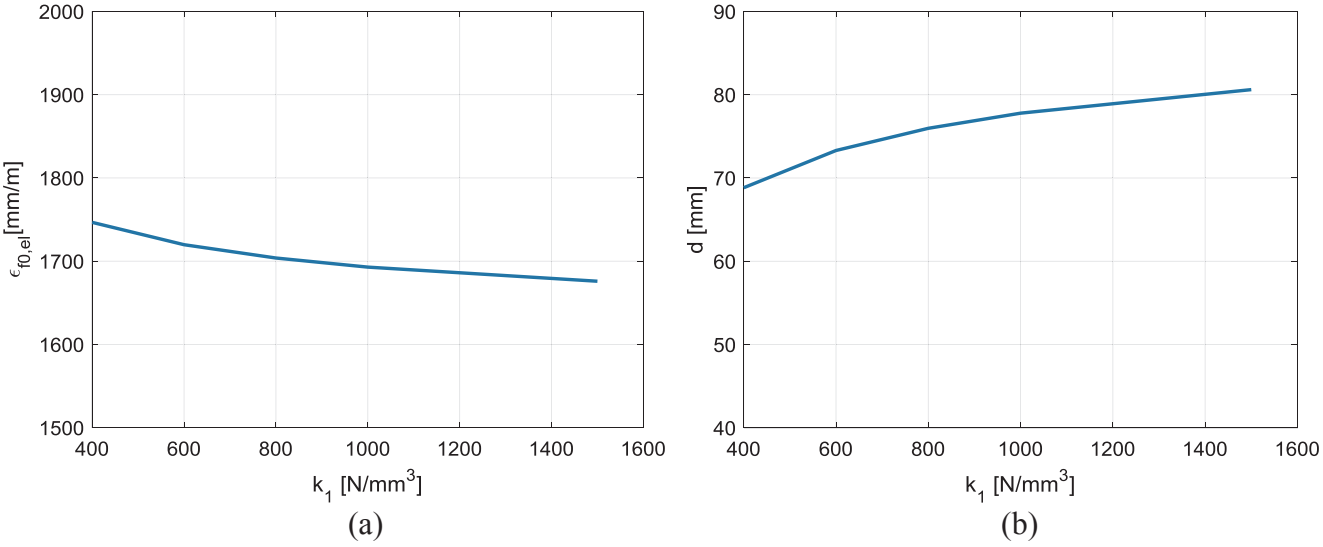

Fig. 11. Effect of the interface elastic stiffness k_1 on (a) the CFRP strain at the elastic limit and (b) the length of the debonded zone.

3.2. Behaviour of the connection interface

The interface response is initially linear and, when a damage criterion is fullfilled, it degrades according to a specific damage evolution law. Two different stages of the interface behaviour can be defined: the elastic behaviour and the damage behaviour. The interface behaviour is described by the relationship between the traction vector $\underline{t}$ and the separation vector $\underline{\delta}$, representing the normal and shear components

3.2.1. Elastic behaviour

In this stage, the contact interaction linear ascending branch was defined by a uncoupled traction-separation model defined by the elastic constitutive matrix $\underline{\underline{K}}$:

$$\underline{t} = \begin{Bmatrix} t_n \\ t_s \\ t_t \end{Bmatrix} = \begin{bmatrix} K_{nn} & 0 & 0 \\ 0 & K_{ss} & 0 \\ 0 & 0 & K_{tt} \end{bmatrix} \begin{Bmatrix} \delta_n \\ \delta_s \\ \delta_t \end{Bmatrix} = \underline{\underline{K}}\underline{\delta} \tag{60}$$

where K_{nn}, K_{ss} and K_{tt} are the elastic stiffnesses in the normal and in the two shear directions, respectively. These elastic stiffnesses are related to the thickness and mechanical properties of the adhesive layer.

3.2.2. Damage behaviour

In this stage, a single damage variable D for the normal, t_n, and the shear tractions, t_t and t_s, is introduced. This means that a strength criterion is needed in order to define the damage initiation. As in [18], the following quadratic strength criterion is adopted:

$$\left(\frac{\langle t_n \rangle}{\overline{\sigma}}\right)^2 + \left(\frac{t_s}{\overline{\tau}}\right)^2 + \left(\frac{t_t}{\overline{\tau}}\right)^2 = 1 \tag{61}$$

where $\overline{\sigma}$ and $\overline{\tau}$ are the interface normal and shear strength, respectively. In general, $\overline{\tau}$ is different in direction s and t. A unique value of $\overline{\tau}$ was considered in Eq. (61) because the same behaviour was assumed in both directions. The symbol $\langle \cdot \rangle$ is the Macaulay bracket, which indicates that compressive stresses do not produce any damage in the interface, that is when t_n is negative it is set equal to zero. When the damage criterion is satisfied, damage occurs and the damage variable D controls the traction vector $\underline{t}$:

$$\widehat{t}_n = \begin{cases} (1-D)\cdot t_n & \text{if } t_n > \overline{\sigma} \\ t_n & \text{otherwise} \end{cases} \tag{62}$$

and

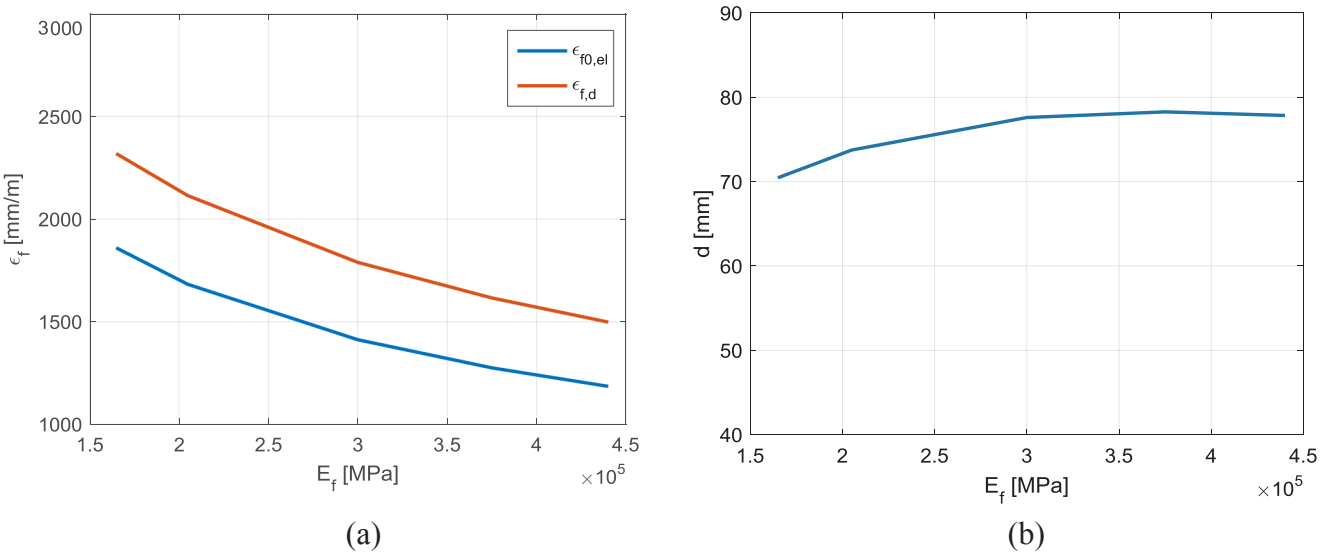

Fig. 12. Effect of the reinforcement Young's modulus on (a) the CFRP strain and (b) the length of the debonded zone.

$$\hat{t}_i = \begin{cases} (1-D)\cdot t_i & \text{if } |t_i| > \bar{\tau} \\ t_i & \text{otherwise} \end{cases} \quad i = s,t \tag{63}$$

where $\bar{\sigma}$ and $\bar{\tau}$ indicate the interface strengths, $\hat{t}_n$ is the damaged normal traction vector component, and $\hat{t}_s$ and $\hat{t}_t$ are the damaged shear and traction vector components. A discrete evolution of the damage variable D was introduced in the finite element code in accordance with the adopted bond-slip relationship (Fig. 5).

4. Validation and parametric analysis

In this section, the analytical and numerical models are calibrated and validated with respect to the outcomes of two different experimental campaigns on cracked steel beam reinforced by using CFRP strips and described in [4,12]. A parametric analysis is also performed to investigate the effects of the crack depth, the parameters of the interface and the stiffness of the reinforcement.

4.1. Validation and calibration of the analytical and numerical models

The results of the analytical and numerical models are compared with the outcomes of two experimental campaigns on cracked steel beams reinforced by using CFRP strips tested under a four-point bending loading configuration.

In [4], the clear span of the I-beams was 1000 mm while the loading points were 500 mm apart. IPE 120 steel beams were used, with a height of 120 mm, a flange width of 64 mm, a flange thickness of 6.3 mm and a web thickness of 4.4 mm. The steel Young's modulus was 210,000 MPa and the beams were artificially notched with an initial crack size of 20 mm at the midspan. The CFRP plate (Sika CarboDur® M614) had a thickness of 1.4 mm, a width of 60 mm and a length of 800 mm. The CFRP Young's modulus was 195,000 MPa.

In [12], the clear span of the I-beams was 1100 mm and the loading points were 200 mm apart. The beams had a height of 120 mm, a flange width of 74 mm, a flange thickness of 8.4 mm and a web thickness of 5 mm. The steel Young's modulus was 205100 MPa and the initial crack length was 14.4 mm. The CFRP plate had a thickness of 1.4 mm, a width of 74 mm and a length of 400 mm. The CFRP Young's modulus was 127,200 MPa.

In both cases, the reinforcement was bonded to the steel beam using the same epoxy adhesive (Sikadur® 30). Results of an experimental campaign described in [26] provided the Young's modulus of the adhesive $E_a = 4500$ MPa, Poisson's ratio $\nu_a = 0.30$, tensile strength $\bar{\sigma} = 25$ MPa and shear modulus $G_a = 1730$ MPa. Different bond–slip relationships were proposed in [18,27,28]. The shear strength, $\bar{\tau}$, was estimated as [18]:

$$\bar{\tau} = 0.9\bar{\sigma} = 22.5MPa \tag{64}$$

while the following bond-slip relationship can be used (Eq. (24)):

$$\delta = \frac{1}{3}\left(\frac{t_a}{G_a}\right)^{0.65}\tau \tag{65}$$

resulting, for an adhesive thickness $t_a = 1$ mm, in an interface elastic stiffness $k_1 = 382$ N/mm^3. Note that, according to Eq. (60), the elastic stiffnesses K_{ss} and K_{tt} in the shear direction are equal to:

$$K_{ss} = K_{tt} = 3\left(\frac{G_a}{t_a}\right)^{0.65} \tag{66}$$

These values were then corrected to best fit the experimental results, following a trial-and-error procedure, resulting in a maximum shear stress $\bar{\tau} = 20$ MPa and an interface elastic stiffness $k_1 = 585$ N/mm^3. Note that the interface elastic stiffness has a marginal influence on the overall response of the reinforced steel beam as it will be shown in Section 4.2 through a parametric analysis. According to Eq. (26), the fracture energy at the interface is equal to 0.3421 N/mm.

4.1.1. Comparison with the experimental results of [4]

Based on the analytical formulation and the numerical simulation presented above, the debonding load is estimated for the geometry and material properties of the reinforced cracked steel beams tested in [4]. The finite element model was created using Abaqus [25] with the dimensions and support conditions given in Fig. 2. General purposes 4-nodes shell elements were used to model both the steel beam and the reinforcement. The adherents were joined defining a proper connection interface as described in Section 3.1. A total of 8665 shell elements was used to model the steel beam, with a typical dimension equal to 6 × 6 mm and with a total number of nodes equal to 8784. A total of 5340 shell elements was used to model the CFRP reinforcement with a typical dimension of 3 × 3 mm for a total number of nodes equal to 5628. The elastic stiffness of the interface K_{nn}, K_{ss} and K_{tt} were assumed to be the same and equal to the stiffness k_1 of the bond-slip relationship ($k_1 = 585$ N/mm^3) while the shear components of interface strength were assumed equal to 20 MPa and the normal component equal to 5 MPa. Finally, in order to avoid convergence issues in the finite ele-ment model, a fictitious softening stage with a large stiffness is in-troduced at the end of the elastic stage. This resulted in a modest

increment of the fracture energy G_f, which entailed for a limited increment of the interface strength.

At first, the midspan deflection of the bare steel beam is computed. The analytical model is based on the rotational spring concept and the midspan deflection is:

$$v = \frac{P_{max} c}{2EI}\left(l^2 - \frac{b^3}{3}\right) + \frac{Pbl}{2k^M} \quad (67)$$

where $P_{max} = 35$ kN is the maximum applied load during the fatigue tests, $c = 250$ mm is the distance between the loading points and the beam supports, $l = 500$ mm is one half of the clear span, EI is the bending stiffness and k_M is the rotational spring stiffness (Eq. (27)). Results from Eq. (67) and from the numerical model are in terms of midspan deflection against the ratio a/h, i.e., the crack depth a normalized with respect to the beam height h (Fig. 7). A strong agreement is observed between the analytical and numerical results showing that the stiffness of the rotational spring k_M was properly estimated in Section 2.1.

Next, the CFRP axial strain distribution is plotted versus the dis-tance x from the midspan (cracked) cross section. In Fig. 8a–d, the numerical and analytical results are compared to the corresponding experimental outcomes (obtained from strain gauge measurements) for different values of the normalized crack length a/h (0.22, 0.3, 0.4, 0.5). In all the cases, the strain gauge readings reveal that a debonded zone is present in the beams. In detail, the CFRP tensile strain is constant over a length of approximately 50 mm for a ratio a/h of 0.22 and gradually increases as the crack length grows up to a CFRP tensile strain constant over a length of approximately 200 mm for a normalized crack length equal to 0.5. The plateau of constant CFRP axial strain is followed by a sharply decreasing axial strain distribution corresponding to the elastic zone. For all the values of a/h, the analytical and numerical models agree very well with the experimental results, both in terms of de-bonded length and axial strain in the debonded zone and with respect to the slope of the axial strain distribution in the elastic zone.

Besides, in the debonded zone, the reinforcement axial strain is independent of the crack length. This is also shown in Fig. 9 where, based on the analytical and numerical models, the axial strain in the debonded zone is plotted against the normalized crack length a/h and compared to the experimental strain gauges readings.

4.1.2. Comparison with the experimental results of [12]

The analytical and numerical models previously discussed are used to estimate the debonding load for the geometry and material properties of the beams experimentally tested by [12]. In this case, the initial crack length is 14.4 mm in all the damaged beams and since the epoxy adhesive was of the same type of the one used in [4], the same bond-slip relationship and numerical parameters for the contact interface response were adopted. The analytical and numerical results from the models discussed in this study are listed in Table 1 and strongly agree with the values of the load at the elastic limit (onset of debonding) experimentally obtained.

4.2. Parametric analysis

Based on the analytical model, a parametric analysis is finally performed to investigate the effect of some design parameters on the CFRP axial strain (both at the elastic limit and after the onset of debonding) and on the debonded zone length. The analysis is performed with reference to the geometry and materials of the steel I-beams investigated in [4]. Accordingly, the load P (Fig. 2) is adopted equal to the maximum applied load during the fatigue tests ($P_{max} = 35$ kN) while the fracture energy at the interface is assumed equal to 0.3421 N/mm (see Section 4.1) and kept constant throughout the parametric analysis. The layout of the parametric analysis is reported in Table 2.

First, the effect of the normalized crack length is investigated. In Section 2.3, it is shown that the axial strain after debonding for a given bending moment, M_0, in the cracked section does not depend on the ratio a/h. Instead, the axial strain at the elastic limit, $\varepsilon_{f,el}$, and the de-bonded zone length d depend on the ratio a/h through the rotational spring stiffness k_M. In Fig. 10a, the CFRP strain at the elastic limit is first plotted as function of the normalized crack length a/h.

It is observed that the normalized crack length has a negligible influence on the axial strain at the elastic limit. In Fig. 10b, the debonded zone length d is plotted versus the normalized crack length a/h and it is observed to drastically increase as the normalized crack length grows. This indicates that debonding is strongly affected by the crack length.

Second, the effect of the interface elastic stiffness k_1 is investigated. In the analytical model, it is observed that the axial strain after the onset of debonding does not depend on k_1. In Fig. 11a and b the CFRP axial strain at the elastic limit, $\varepsilon_{f,el}$, and the debonded zone length, d, is plotted versus the elastic stiffness k_1 showing that the interfacial elastic stiffness has a marginal influence on both factors.

Then, the reinforcement Young's modulus and its effect on the axial strain and the length of the debonded zone is considered. In Fig. 12a, based on the analytical model (Eqs. (56) and (57)), the axial strain at the elastic limit and after the onset of debonding is plotted versus the reinforcement elastic stiffness E_f. It is thus clearly observed that in both cases the axial strain tends to decrease as the reinforcement elastic stiffness E_f increases.

Finally, the Young's modulus of the CFRP reinforcement and its effect on the debonded zone length d is analyzed. In Fig. 12b, the de-bonded zone length is plotted with respect to the reinforcement elastic stiffness E_f and it can be noticed that the Young's modulus of the CFRP reinforcement has a marginal effect on this parameter.

5. Conclusions

In this paper, cracked steel beams strengthened by using composite materials under fatigue loads were studied. On the basis of the outcomes of an experimental campaign on artificially notched I-shaped steel beams strengthened with CFRP reinforcements [4] and through the development of an analytical formulation and of a numerical model accounting for a cohesive interface between the composite and the steel substrate, the main aim and novelty of this study is to estimate how the fatigue crack propagation (in terms of crack length) is strictly related and influenced by the progressive debonding of the reinforcement. In detail:

(a) Among the experimental findings on the fatigue behaviour of artificially notched steel beams strengthened with CFRP plates [4], strain gauges measurements revealed the presence of a debonded area between the reinforcement and the steel substrate close to the crack location.
(b) Analytical models were previously developed in [4,10]. The originality of the more refined analytical model proposed in this work consists in the fact that it is not only able to evaluate the CFRP axial force but also to predict the debonded zone length. The analytical formulation was calibrated and validated with respect to the experimental outcomes presented in [4,12]. An extremely good agreement is observed.
(c) A numerical finite element model, employing a damaging cohesive interface, was presented. The advantage of this model, with respect to the (FE) simulations proposed in [4], relies on the possibility to follow the progressive debonding of the reinforcement for a certain crack length and under an increasing load. The FE model was also employed for the validation of the analytical results and a good agreement was found.
(d) Finally, based on the analytical model, a parametric analysis was performed to investigate the influence of the most relevant parameters on the strain distribution in the reinforcement layer. In detail, the crack length in the notched steel beam does not influence

the axial strain along the debonded zone but marginally affects the axial strain at the elastic limit and strongly influences the debonded zone length. The same holds for the elastic stiffness at the interface. The Young's modulus of the CFRP reinforcement has a marginal effect on the debonded zone length and it is observed that as the reinforcement elastic stiffness increases the axial strain in the CFRP tends to decrease.

Acknowledgements

The financial support of the Politecnico Milano 1863 is gratefully acknowledged by the authors.

References

[1] Zhao XL. FRP-strengthening metallic structures. Boca Raton, London, New York: CRP Press, Taylor & Francis Group; 2014.
[2] Ghafoori E, Motavalli M, Botsis J, Herwig A, Galli M. Fatigue strengthening of damaged metallic beams using prestressed unbonded and bonded CFRP plates. Int J Fatigue 2012;44:303–15.
[3] Wu G, Wang HT, Wu ZS, Liu HY, Ren Y. Experimental study on the fatigue behavior of steel beams strengthened with different fiber-reinforced composite plates. J Compos Constr 2012;16(2):127–37.
[4] Colombi P, Fava G. Experimental study on the fatigue behavior of cracked steel beams repaired with CFRP plates. Eng Fract Mec 2015;145:128–42.
[5] Yu QQ, Wu YF. Fatigue strengthening of cracked steel beams with different configurations and materials. J Compos Constr 2017;21(2):04016093.
[6] Yu QQ, Wu YF. Fatigue durability of cracked steel beams retrofitted with high-strength materials. Constr Build Mat 2017;155:1188–97.
[7] Dunn ML, Suwito W, Hunter B. Stress intensity factors for cracked I-beams. Eng Fract Mech 1997;57(6):609–15.
[8] Ghafoori E, Motavalli M. Analytical calculation of stress intensity factor of cracked steel I-beams with experimental analysis and 3D digital image correlation measurements. Eng Fract Mech 2011;78(18):3226–42.
[9] Hmidan A, Kim YJ, Yazdani S. Stress intensity factors for cracked steel girders strengthened with CFRP sheets. J Compos Constr 2014;19(5):04014085.
[10] Colombi P, Fava G. Fatigue crack growth in steel beams strengthened by CFRP strips. Theor Appl Fract Mech 2016;85:173–82.
[11] Zheng B, Dawood M. Fatigue crack growth analysis of steel elements reinforced with shape memory alloy (SMA)/fiber reinforced polymer (FRP) composite patches. Compos Struct 2017;164:158–69.
[12] Deng J, Jia Y, Zheng H. Theoretical and experimental study on notched steel beams strengthened with CFRP plate. Compos Struct 2016;136:450–9.
[13] Stratford T, Cadei J. Elastic analysis of adhesion stresses for the design of a strengthening plate bonded to a beam. Constrand Build Mat 2006;20:34–45.
[14] Deng J, Lee MMK. Behaviour under static loading of metallic beams reinforced with a bonded CFRP Plate. Compos Struct 2007;78:232–42.
[15] Cornetti P, Corrado M, De Lorenzis L, Carpinteri A. An analytical cohesive crack modeling approach to the edge debonding failure of FRP-plated beams. Int J Solids Struct 2015;53:92–106.
[16] Bocciarelli M, Colombi P, Fava G, Sonzogni L. Energy-based analytical formulation for the prediction of end debonding in strengthened steel beams. Compos Struct 2016;153:212–21.
[17] Liu M, Dawood M. A closed-form solution of the interfacial stresses and strains in steel beams strengthened with externally bonded plates using ductile adhesives. Eng Struct 2018;154:66–77.
[18] Teng JC, Fernando D, Yu T. Finite element modelling of debonding failures in steel beams flexurally strengthened with CFRP laminates. Eng Struct 2015;86:213–24.
[19] Kianmofrad F, Ghafoori E, Elyasi MM, Motavalli M, Rahimian M. Strengthening of metallic beams with different types of pre-stressed un-bonded retrofit systems. Compos Struct 2017;159:81–95.
[20] Kim YJ, Brunell G. Interaction between CFRP-repair and initial damage of wide-flange steel beams subjected to three-point bending. Compos Struct 2011;93(8):1986–96.
[21] Hmidan A, Kim YJ, Yazdani S. CFRP repair of steel beams with various initial crack configurations. J Compos Constr 2011;15(6):952–63.
[22] Kim YJ, Harries KA. Predictive response of notched steel beams repaired with CFRP strips including bond-slip behaviour. Int J Struct Stab 2012;12(1):1–21.
[23] Wang J. Cohesive zone model of intermediate crack-induced debonding of FRP-plated concrete beams. Int J Solids Struct 2006;43:6630–48.
[24] Wang J. Deboning of FRP-plated reinforced concrete beams, a bond slip analysis. I Theoretical formulation. Int J Solids Struct 2006;43:6649–64.
[25] Simulia. 2016. Abaqus 6.13 extended functionality online documentation (generated January 15, 2016).
[26] Fava G. Strenghtening of metallic structures using carbon fiber reinforced polymer materials. Ph.D. thesis, Politecnico di Milano – Department of Structural Engineering; 2007.
[27] Xia SH, Teng JG. Behaviour of FRP-to-steel bonded joints. In: Proceedings of the international symposium on bond behaviour of FRP in structures (BBFS2005), Hong Kong; 2005. p. 419–26.
[28] Fawzia S, Zhao XL, Al-Mahaidi R. Bond–slip models for double strap joints strengthened by CFRP. Compos Struct 2010;92(9):2137–45.